RSC
Mechanochemistry

ROYAL SOCIETY OF CHEMISTRY

PAPER

View Article Online
View Journal

Check for updates

Cite this: DOI: 10.1039/d5mr00147a

Sign of mechanochemical curvature governing O_2 activation mechanisms and reactivity on rippled supports

Sayan Banerjee *

Received 2nd December 2025
Accepted 9th March 2026

DOI: 10.1039/d5mr00147a

rsc.li/RSCMechanochem

Two-dimensional (2D) materials are inherently prone to forming ripples and wrinkles that create regions of nonzero curvature – a mechanochemical landscape arising from intrinsic deformation – thereby modulating their electronic structure and a range of associated properties. Such curvature effects have implications for stability, quantum processes, and adsorption phenomena. The influence of curvature—treated as a vector descriptor distinguishing positive and negative curvature—on reactivity remains underexplored, particularly in the context of small-molecule activation and multistep catalytic reactions. Here, we investigate rippled N-doped graphene and quantify how curvature, viewed as a local mechanochemical deformation, modulates O_2 reactivity on single-atom sites, denoted as M–N–C (M = Fe, Co, Mn, Pt), using density functional theory. We find that the sign of curvature determines the O_2 activation mode: for Mn and Fe, negatively curved regions (mountain-shaped) favor an η^2 side-on configuration, whereas positively curved regions (valley-shaped) promote an η^1 end-on mode. In contrast, Co and Pt exhibit only curvature-independent η^1 binding. The η^2 mode observed for Fe and Mn resembles molecular O_2 adducts in transition-metal complexes. Curvature-dependent charge transfer enhances electron donation at negatively curved sites, facilitating O_2 activation. We establish curvature-resolved scaling relations for oxygen reduction reaction (ORR) intermediates (OOH, O, and OH), highlighting where the global linear relationships remain valid and where they break down when curvature is introduced as a geometric variable. The sign of curvature also modulates ORR overpotentials: positive curvature regions yield lower overpotentials, whereas negative curvature sites lead to higher values for Fe and Mn. Consequently, we predict that negatively curved, mountain-like sites can be engineered for O-atom transfer reactions to organic substrates, which compete with ORR under electrochemical conditions. Finally, we show that variable curvature further influences the overpotential by enabling different ORR steps at varying curvatures on a corrugated surface. Overall, curvature can be harnessed to enable distinct reactivity from identical catalytic motifs, underscoring the importance of incorporating dynamic curvature effects in future theoretical and experimental studies.

Introduction

Two-dimensional (2D) materials, including carbon-based systems such as graphene and graphite, as well as transition-metal dichalcogenides (TMDs), exhibit ripples and wrinkles that spontaneously form regions with nonzero curvature.[1–4] Curvature couples mechanical deformation with electronic structure by introducing strain gradients, thereby providing a means to tune electronic structure properties with implications for optoelectronics and catalysis.[2,5–7] Both free-standing and supported single-layer systems, with and without defects, have been reported to exhibit ripples.[1,8,8,9,9–16] Moiré-type materials, which exploit geometric tunability of electronic localization, have also been shown to influence adsorption energetics on graphitic surfaces.[17,18] In the presence of defects, adsorbates, or supporting substrates, the degree of corrugation can vary further. However, the role of curvature as a vector descriptor in influencing multistep catalytic reactions remains underexplored.

Single-atom catalysts (SACs) supported on two-dimensional N-doped graphene, referred to as M–N–C catalysts, are known to mediate multistep small-molecule transformations such as the oxygen reduction reaction (ORR), CO_2 reduction (CO_2RR), and related processes.[19,20] In such multistep catalytic transformations, scaling relations between reaction intermediates remain largely valid even under varying external conditions, including thermal, electrochemical, and photocatalytic environments.[21] Overcoming these scaling relations is therefore a central goal in the rational design of next-generation catalysts.[22] Approaches to modify these relations often involve tuning the geometric and electronic structure of the active site through catalyst design or external stimuli.[23–25] Strain

---

Department of Chemistry, University of Tennessee, Knoxville, TN 37923, USA. E-mail: sbanerjee@utk.edu

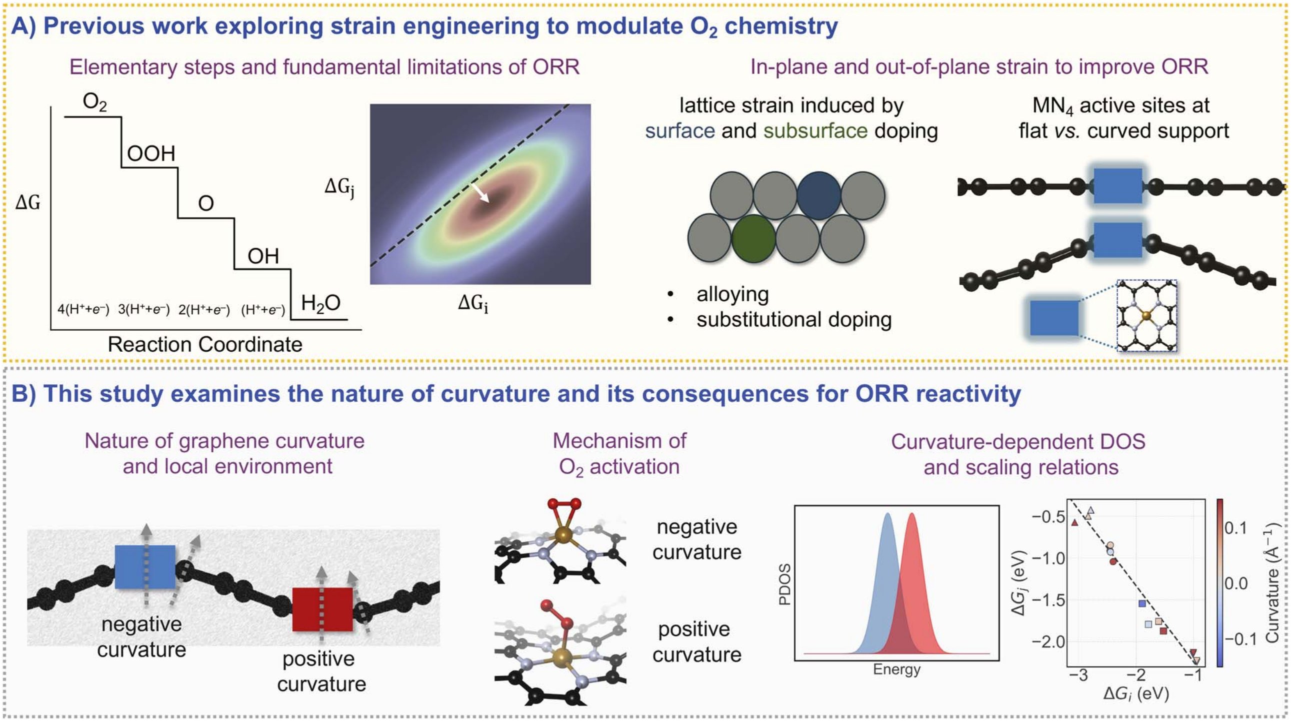

Fig. 1 (A) Schematic overview of the oxygen reduction reaction (ORR) steps and the influence of strain on ORR energetics. (B) Summary of this study highlighting how curvature can be exploited to achieve facile O_2 activation and curvature-dependent scaling relations.

engineering, in particular, alters the local electronic structure by redistributing charge density and modifying bond polarity (Fig. 1A).[26–28] Nevertheless, the role of curvature—particularly the distinction between positive (valley) and negative (mountain) curvature—on catalytic thermodynamics and scaling relations remains underexplored. Existing studies often treat curvature as a scalar quantity, such as the radius of curvature, implicitly assuming a monotonic effect.[29–33] Such simplifications neglect the geometric and electronic distinctions between negative curvature (mountain-like) and positive curvature (valley-like) regions, which create distinct surface–adsorbate environments (Fig. 1B).

Out-of-plane deformation, or curvature, has received limited attention in the context of small-molecule activation and multistep catalytic transformations. Here, we investigate how the nature of curvature influences such processes using O_2 reactivity and the ORR as a model system.[22,34] The ORR serves as an ideal benchmark because its scaling relations and theoretical overpotentials are well established across many catalytic systems, enabling quantitative assessment of reactivity trends when curvature is introduced as a vector variable.

In this work, we systematically examine how the nature and magnitude of curvature affect O_2 adsorption, activation, and the resulting scaling relations in M–N–C single-atom catalysts (Fig. 1). Using first-principles density functional theory (DFT), we investigate a series of M–N–C sites (Fe, Co, Mn, Pt), where earth-abundant metals are selected to assess curvature effects on O_2 chemistry, and Pt is included as a reference to represent weakly interacting sites.[35–40] Curvature differentially influences O_2 activation across metals, producing curvature-dependent binding for Fe and Mn and curvature-independent binding for Co and Pt. Specifically, η^2 side-on O_2 binding occurs at Fe and Mn sites under negative curvature, resembling O_2 coordination observed in molecular catalysts. In contrast, positively curved Mn and Fe sites, as well as all Co and Pt sites, favor η^1 end-on binding. Curvature-modified scaling relations of ORR intermediates highlight both the bonding patterns for which linear scaling remains largely valid and the cases where deviations emerge when η^2 O_2 binding is achieved, providing a route to exploit this mode for O-atom transfer reactions. Furthermore, we find that curvature modulates the ORR overpotential, with positive curvature yielding lower values. Finally, we introduce the concept of variable curvature coupling, wherein reaction steps occur across multiple curvature-defined sites. These results suggest that on real, corrugated surfaces, the measured catalytic activity arises from a collective response of regions with varying curvature. Overall, this study establishes curvature as a fundamental descriptor of reactivity in 2D catalysts and motivates experimental investigations combining electrochemistry and spatially resolved microscopy to probe curvature-dependent catalytic behavior on surfaces.

Results and discussion

Curvature-dependent O_2 binding

We first evaluated the O_2 binding energy (ΔE_{O_2}) as a function of curvature by considering $M–N_4$ active sites[20,41,42] embedded in a sinusoidally curved N-doped graphene framework with varying curvature magnitude and sign (Fig. 1B and left panel in Fig. 2A). Calculations were performed for four representative M–N–C single-atom sites in the M–N$_4$ geometry, where the metal center (M) is Mn, Fe, Co, or Pt. O$_2$ adsorption on Co and Pt shows negligible dependence on curvature, with the η^1 end-on binding mode preserved across all curvature values (Fig. 2A and B). In contrast, Mn and Fe exhibit a significant curvature dependence: regions at negative curvature (mountain) favor stronger O$_2$ adsorption and enhanced activation compared to regions at positive curvature (valley). The preference for η^2 binding modes, particularly for Fe and Mn, is further corroborated by calculating the relative preference between η^1 and η^2 binding modes at high negative curvature (-0.12 Å^{-1}, mountain) and high positive curvature ($+0.12$ Å^{-1}, valley) through constrained optimization. In other words, we quantify the feasibility of switching between η^2 and η^1 binding modes and how this depends on curvature. We find that for Fe and Mn, η^1 is more preferred than η^2 at the valley, whereas (as stated in Fig. 2A and B) η^2 is more preferred than η^1 at the mountain. In contrast, for Co and Pt, η^1 is more preferred than η^2 at both the valley and the mountain (see Fig. S2 for more details).

Mn and Fe sites at negative curvature provide greater geometric flexibility and stronger electrostatic interactions, enabling η^2 side-on O$_2$ coordination and thereby facilitating O–O bond activation (Fig. 2B). The optimized geometries at these sites closely resemble those reported experimentally for side-on O$_2$ activation in molecular Mn and Fe complexes.[43,44] Moreover, the η^2 binding mode leads to a higher spin state compared to the η^1 configuration, consistent with the molecular analogy between peroxo- and superoxo-type O$_2$ activation mechanisms. These results demonstrate that, in heterogeneous systems, curvature can be exploited to access distinct binding modes—analogous to how ligand design modulates coordination motifs in molecular catalysis.

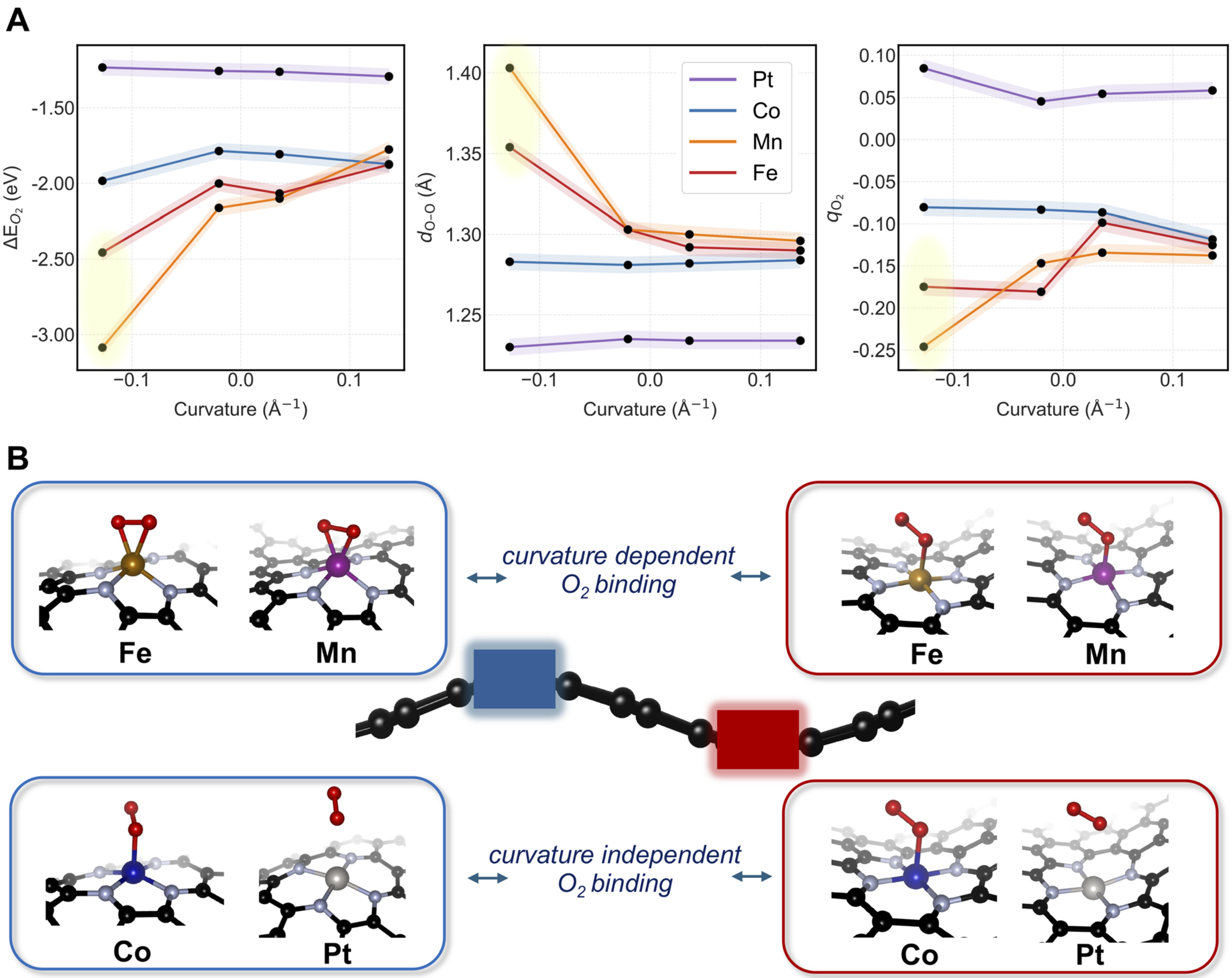

Fig. 2 (A) Left panel: Curvature-dependent O$_2$ binding at MN$_4$ sites of M–N–C catalysts (M = Mn, Fe, Co, and Pt). Middle and Right panel: variation of O–O bond length (d_{O-O}) and total charge on O$_2$ (q_{O_2}) in the O$_2$-adsorbed geometries as a function of curvature. (B) Curvature-dependent O$_2$ binding motifs. For Mn and Fe, η^2 side-on binding occurs at regions of higher negative curvature, whereas η^1 end-on binding is observed at all other curvature values. Data points corresponding to η^2 O$_2$ binding motifs are highlighted in yellow. Color code: C (black), N (light blue), Fe (golden brown), Mn (purple), Pt (silver).

To quantify the extent and origin of O_2 activation, we analyzed the O–O bond lengths and Löwdin charges in the adsorbed configurations (Fig. 2B). In Fig. 2A, we plot the O–O bond length (d_{O-O}) and the total charge on O_2 (q_{O_2}) as functions of curvature to elucidate the origin of the O_2 binding trends. We find that stronger O_2 binding correlates with elongated O–O bonds, with distinct differences between the η^1 and η^2 coordination modes. For η^1 binding, the O–O bond length remains below 1.30 Å, and Pt exhibits the weakest O_2 activation, consistent with the known limitation of Pt in activating molecular oxygen.[27] In contrast, for the η^2 activation mode, the O–O bond length extends to 1.40 Å and 1.35 Å for Mn and Fe, respectively. For comparison, O–O bond lengths of 1.41 Å and 1.32 Å have been reported for molecular Mn and Fe catalysts with N-based coordination environments,[43] consistent with the values obtained for the curved MN_4 sites.

Furthermore, the η^2 configurations exhibit enhanced charge transfer from the metal center to the adsorbed O_2, resulting in more negative q_{O_2} values (right panel in Fig. 2A). Overall, the extent of charge transfer depends strongly on the nature of curvature, with Mn and Fe showing a more pronounced dependence than Co and Pt. This trend can be attributed to the relatively higher ionic character of Mn and Fe, where electrostatic interactions dominate metal–O_2 coupling. Conversely, the later transition metals, such as Co and Pt, lack electrostatic favorability, resulting in weaker sensitivity to geometric distortion. Overall, these results demonstrate that the nature of curvature modulates charge transfer, thereby controlling the O_2 binding strength, activation pathway, and overall degree of O_2 activation.

Curvature-dependent binding energy and scaling relations

Fig. 3 illustrates the curvature-dependent binding energy and associated scaling relations of the ORR intermediates (O, OH, OOH, and O_2) for representative M–N–C single-atom catalysts (Fe, Co, Mn, and Pt). Each panel compares the adsorption energies (ΔE) of two intermediates, with data points color-coded according to curvature (red for positive and blue for negative curvature). For metals with strong curvature dependence (Fe and Mn), adsorption is consistently stronger at more negative curvature (mountain) than at more positive curvature (valley). For metals with weak curvature dependence (Co and Pt), this systematic mountain–valley trend is not observed.

The binding energies of OOH, O, and OH are correlated, indicating that the nature of bonding remains consistent for these intermediates across curvature types. The correlations involving ΔE_{O_2} weaken due to the η^2 O_2 binding motifs at negative curvature for Fe and Mn (yellow in Fig. 3), indicating that a change in O_2 bonding mode affects the overall scaling relations. The extent to which curvature perturbs adsorption energetics varies among metals, as shown in Fig. 3. Early transition metals such as Fe and Mn exhibit more pronounced curvature sensitivity, showing larger changes in adsorption energies with curvature for all intermediates. In contrast, Co and Pt display minimal dependence on curvature, irrespective of the intermediate considered. This behavior suggests that, under experimental conditions, Co- and Pt-based active sites are less susceptible to geometric perturbations and dynamic fluctuations than Fe and Mn.

When data from both positive and negative curvature regions are considered together, a single universal scaling relation emerges, encompassing all curvature regimes. Therefore, we report curvature-modified scaling relationships for the binding energies of OOH, O, and OH.[34,45–47] Next, we compare the slopes with literature values reported for ORR and assess the impact of curvature on these relationships. Notably, the slope of the OOH–OH correlation is 0.91, close to unity across all metals and curvature magnitudes, indicating a similar metal–oxygen bonding character for these two intermediates throughout the curvature range. The near-unity slope is consistent with octet/electron-counting arguments, since both *OH and *OOH lack one electron to reach the octet. In contrast, the OH–O correlation exhibits an approximate slope of 0.5, reflecting the transition from predominantly single-bond character in OH adsorption to partial double-bond character in atomic O adsorption. In other words, oxygen in *OH lacks one electron to reach the octet, whereas *O lacks two electrons. Furthermore, the slope for the OOH–O correlation is ~0.5, matching the expected value associated with established scaling relations.[34,45–47] Overall, these slope values are consistent with previously established ORR scaling relations for metal and M–N–C catalysts,[34,45–47] indicating that curvature preserves the fundamental nature of metal–oxygen bonding.

Although the scaling relations hold reasonably well across metals, adsorbates, and curvature regimes, we find indications that they can break down when curvature induces a more nontrivial perturbation of bonding—most notably for O_2 binding. Full metal-specific scaling parameters are provided in the SI (Table S1, and Fig. S3–S6). For all scaling pairs involving O_2, the corresponding data points systematically extend beyond the spread defined by the other adsorbates—even within a given metal—indicating a clear deviation from the otherwise near-linear trends (Fig. 3). As discussed in terms of reactivity (*vide infra*), these outlying O_2 points therefore signal a breakdown of scaling behavior. This deviation also manifests as metal-dependent scaling for O_2-involving relations, *i.e.*, a breakdown of a single global scaling line. The effect is pronounced for ΔE_O *versus* ΔE_{O_2}, where metals exhibiting strong curvature sensitivity (Fe and Mn) follow a different slope than metals with weaker curvature response (Co and Pt). This interpretation is reinforced by metal-specific regressions: the fitted slopes naturally cluster into strong-curvature (Fe and Mn) and weak-curvature (Co and Pt) regimes, consistent with curvature-driven changes in bonding being qualitatively different across these two regimes (Table S1). This opens a route to selectively harness O_2 activation to drive chemical transformations that are not typically accessible under reducing, ORR-relevant conditions, where conventional scaling constraints tend to enforce correlated adsorption energetics and limit independent tuning of key intermediates.

Effect of curvature on electronic structure

Next, we examine how curvature influences the electronic structure and, consequently, the binding energy trends. In the

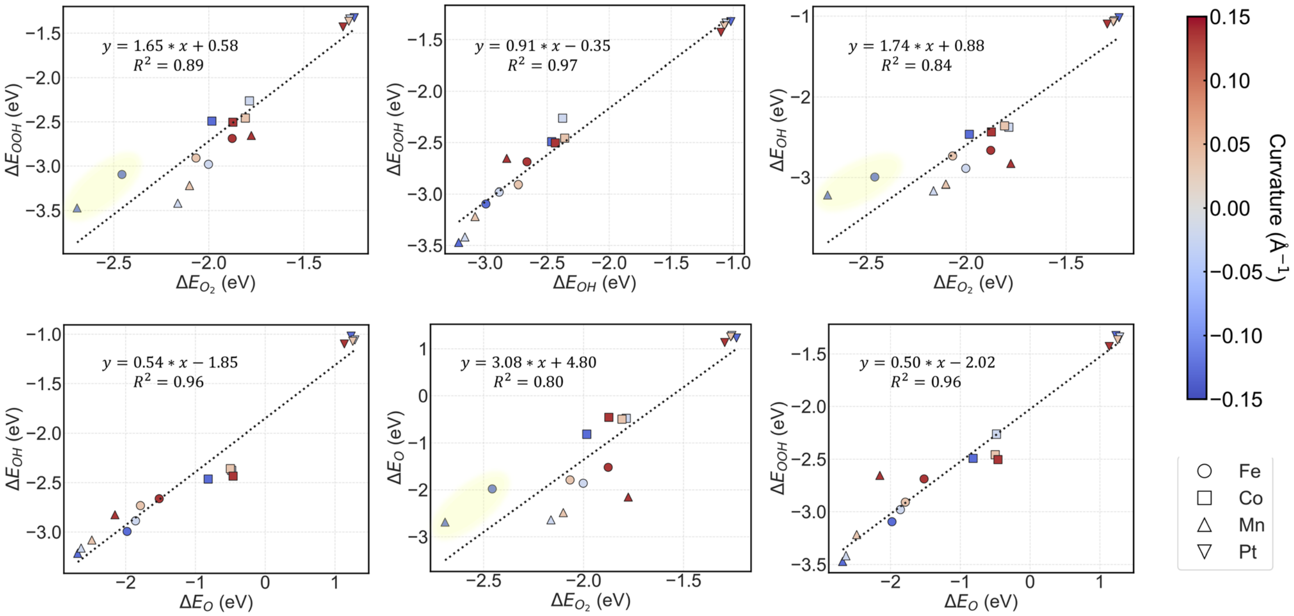

Fig. 3 Curvature-dependent binding energies and scaling relations among oxygen reduction reaction (ORR) intermediates (O_2, OOH, O, and OH) for M–N–C single-atom catalysts. Each panel shows the correlation between the binding energies (ΔE) of two intermediates for Fe, Co, Mn, and Pt, with data points color-coded by curvature (red for positive and blue for negative curvature). The dashed diagonal line is the linear scaling relation. Data points corresponding to η^2 O_2 binding motifs are highlighted in yellow, reflecting their outlier character.

absence of an adsorbate, the nature of curvature has no physical significance, as adsorption itself breaks the symmetry between mountain and valley regions. Therefore, all analyses presented here correspond to adsorbed configurations. The objective of this analysis is explanatory rather than predictive—aimed at identifying the electronic factors that are modulated under curvature. Linear regression (LR) models were constructed using five key type of electronic structure descriptors: the metal *d*-band center ε_d, the oxygen *p*-band centers ε_p, and PDOS overlap metrics S evaluated over different energy windows (total, occupied, and unoccupied) to probe the nature of metal–oxygen bonding.

We perform metal-specific regression (*i.e.*, separate models for Fe, Mn, Co, and Pt) rather than a global model across metals, so that the fitted coefficients reflect the curvature response within a given metal. Model selection and full statistical metrics (including R^2 values for descriptor combinations) are reported in the SI (Fig. S2). In addition, we also report global adsorbate-specific models (*i.e.*, LR models that include all four metals) in the SI (Fig. S7–S9); however, these global fits do not capture metal-specific trends and provide limited chemical insight into how electronic-structure descriptors respond to curvature for different metals, particularly in cases where the curvature effect is strong (Fe and Mn) *versus* weak (Pt and Co).

To compare descriptor sensitivities across metals on the same scale, descriptor values are normalized prior to fitting. We summarize curvature sensitivity using the absolute magnitude of the fitted coefficients, $|c|$, from the best-performing normalized models for each metal–adsorbate pair (Fig. 4A). The best-performing models are either single-descriptor or two-descriptor forms, selected based on predictive performance; when the single-descriptor model yields $R^2 < 0.6$, we report the values associated with two-descriptor models. For two-descriptor models, we report the average absolute coefficient magnitude (Fig. 4A). All model details and results are provided in the SI (Table S2).

We find systematically larger coefficient magnitudes associated with the electronic structure descriptors in the constructed LR models (Fig. 4A) for Mn and Fe across adsorbates, whereas Co and Pt exhibit smaller coefficients, indicating a weaker curvature-driven modulation of the electronic descriptors (Fig. 4A). It is worth noting that the O_2 binding mode difference can also be captured through these coefficients, as can be seen from high coefficients associated with the LR models for Mn and Fe, than Co and Pt. In other words, the outlier nature can be captured from the electronic structure descriptors of the binding modes, implicating it has clear electronic structure connection. Collectively, these LR models establish that electronic structure properties vary systematically under curvature, and that the magnitude of this response is correlated with the influence of curvature on binding-energy trends.

We further relate descriptor-based coefficients to the magnitude of curvature effects on adsorption energetics. In Fig. 4B we plot $|c|$ against the binding-energy range $\Delta E_{\mathrm{range}}$ spanned across curvatures for each adsorbate. Across metals, larger $|c|$ is associated with larger $\Delta E_{\mathrm{range}}$, linking the curvature dependence of adsorption energetics to the curvature dependence of the underlying electronic descriptors. This coefficient–range relationship provides a quantitative way to compare curvature sensitivity across metals and intermediates using physically motivated electronic structure measures.

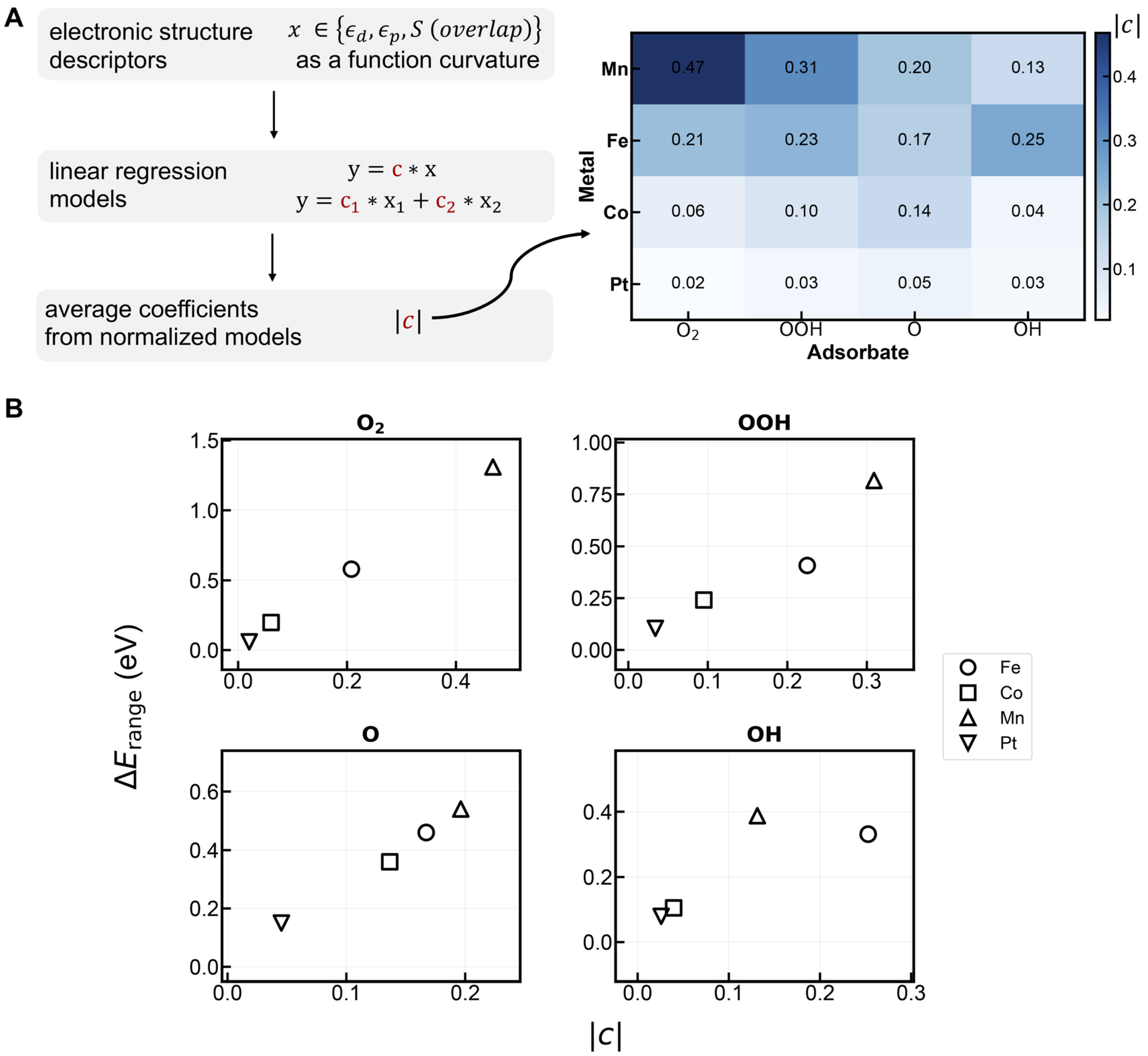

Fig. 4 Metal-specific linear regression analysis linking curvature-driven electronic-structure changes to binding-energy variations. (A) Curvature-dependent electronic-structure descriptors ($x \in \{\varepsilon_d, \varepsilon_p, S\}$, where S denotes the PDOS overlap metric) were used to construct metal-specific linear regression models (one- and two-descriptor forms). Descriptor values were normalized prior to fitting to enable comparison of coefficient magnitudes across metals. The heat map reports the absolute coefficient magnitude, $|c|$, of the normalized LR models for each metal–adsorbate pair, quantifying descriptor sensitivity to curvature. (B) Relationship between electronic-structure sensitivity and curvature-driven binding-energy variation. For each adsorbate (O_2, OOH, O, and OH), the binding-energy range across curvature, ΔE_{range}, is plotted against $|c|$ for each metal (Fe, Co, Mn, and Pt), showing that larger coefficient magnitudes are associated with larger curvature-induced binding-energy ranges.

Overall, the metal-dependent curvature response (*i.e.*, strong *vs.* weak curvature effects) can be traced to corresponding changes in electronic structure, providing a physical interpretation of these trends. Pt exhibits the weakest curvature dependence: the corresponding LR models are dominated by small coefficients for descriptors based on either ε_d of metal or ε_p of O, consistent with limited curvature-driven variation in metal–adsorbate bonding. In contrast, for metals exhibiting strong curvature effects (Mn and Fe), overlap descriptors S appear consistently among the best-performing models and carry comparatively larger coefficients, indicating that curvature more strongly perturbs hybridization-related bonding measures. Thus, curvature-driven changes in fundamental bonding indicators connect the observed modifications in electronic structure to the corresponding curvature dependence of binding energies.

Curvature-dependent overpotential

Fig. 5 extends the curvature-dependent adsorption analysis (Fig. 3) to the corresponding reaction free energies (ΔG) of the elementary ORR steps (see Methods). ΔG defines the four proton–electron transfer steps in the ORR pathway and collectively determines the limiting potential (U_L) and the theoretical overpotential (η_{theo}).[22,34]

The free-energy relations among the ORR intermediates (Fig. 5) exhibit consistent linear trends across metals and curvature regimes, similar to those in Fig. 3. Specifically, ΔG_{OOH} and ΔG_O correlate positively, indicating that sites with stronger OOH binding also stabilize O intermediates. In contrast, ΔG_{OOH} correlates negatively with both ΔG_{OH} and ΔG_{H_2O}, reflecting that stronger binding in the early ORR steps leads to less exergonic protonation in the later stages. Finally, ΔG_{OH} and ΔG_{H_2O} show a positive correlation, consistent with their similar metal–oxygen bonding motif in the OH* geometry.

Positive curvature corresponds to less exergonic ΔG values—*i.e.*, weaker adsorption and energetics closer to the optimal thermodynamic window of 1.23 eV per proton–electron transfer step. Conversely, negative curvature enhances O_2 and OOH binding, producing more negative ΔG_{OOH} and ΔG_O values. This stronger initial adsorption renders subsequent steps, such as OH* formation and the second H_2O formation, less exergonic, thereby determining the limiting potential and overall overpotential. For Fe and Mn, step-3 (O* to OH* conversion) and step 4 (OH* to H_2O conversion) emerges as the limiting potential step. For Co and Pt, however, the intrinsically weaker O binding makes the OOH formation step rate-determining across all curvature regimes, consistent with its weak O_2 adsorption.

The η_{theo} values across different curvatures show metal-specific trends. As shown in Fig. 6A, Fe- and Mn-based systems exhibit curvature dependence, with η_{lim} increasing systematically as curvature becomes more negative. In contrast, Co and Pt display minimal variation in η_{theo} across the curvature range, indicating reduced sensitivity to geometric distortion. For Mn and Fe, positive curvature (valley-like regions) generally corresponds to lower overpotentials, whereas negative curvature (mountain-like regions) results in higher η_{theo}. This behavior originates from the overbinding of early ORR intermediates—particularly O_2^* and OOH*—at negatively curved sites, which makes subsequent protonation steps thermodynamically less favorable. The weaker binding at positively curved regions aligns adsorption energetics more closely with the ideal thermodynamic window, leading to lower η_{theo}.

Overall, the curvature dependence of η_{theo} establishes a geometric design principle for optimizing catalytic activity on curved surfaces: regions of positive curvature are more favorable for achieving high ORR performance. In contrast, negatively curved sites, characterized by stronger O_2 binding and higher η_{theo}, exhibit lower ORR activity but may serve as promising active sites for O-atom transfer reactions to organic substrates, which often compete with ORR under electrochemical conditions. We therefore predict that on uneven or dynamically corrugated surfaces, negatively curved regions can promote selective O-atom transfer, whereas positively curved regions remain the most active toward ORR.

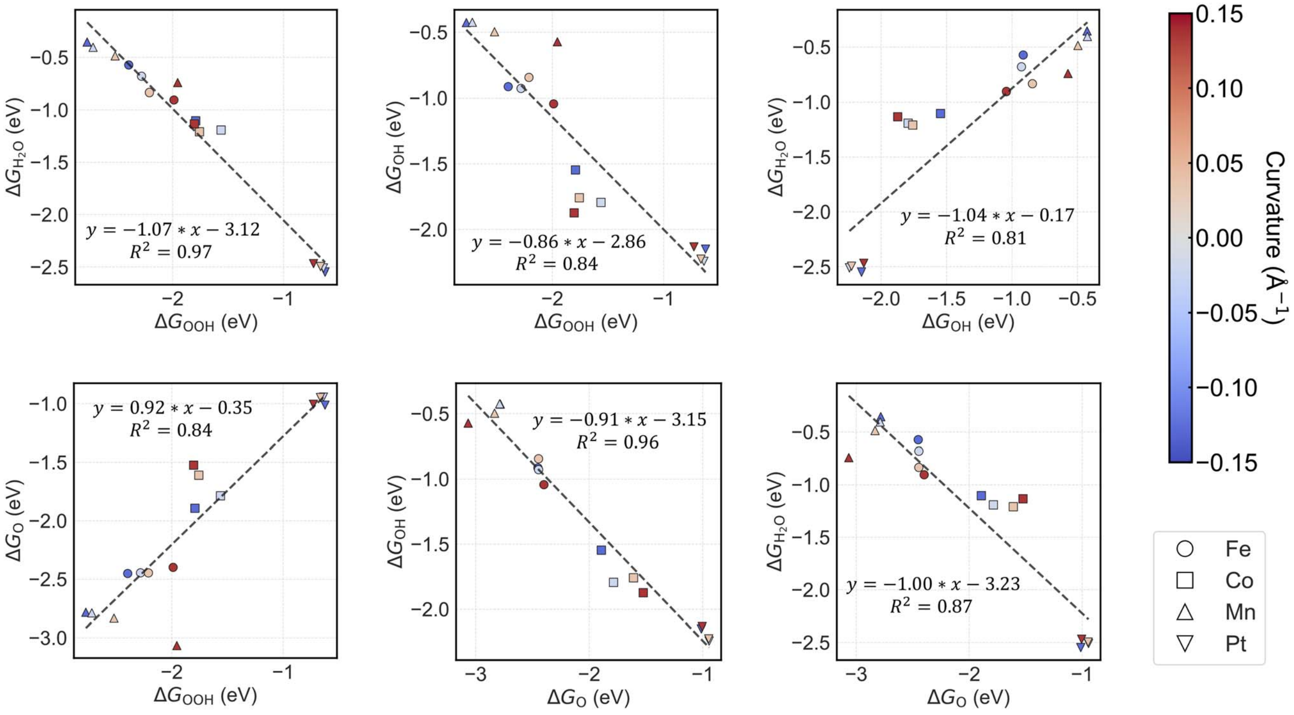

Fig. 5 Curvature-dependent scaling relations among the reaction free energies (ΔG) of ORR intermediates for representative M–N–C single-atom catalysts (Fe, Co, Mn, and Pt). Each panel compares the free energies of two intermediates, with data points color-coded according to curvature (red for positive and blue for negative curvature). The dashed line represents the linear scaling relation.

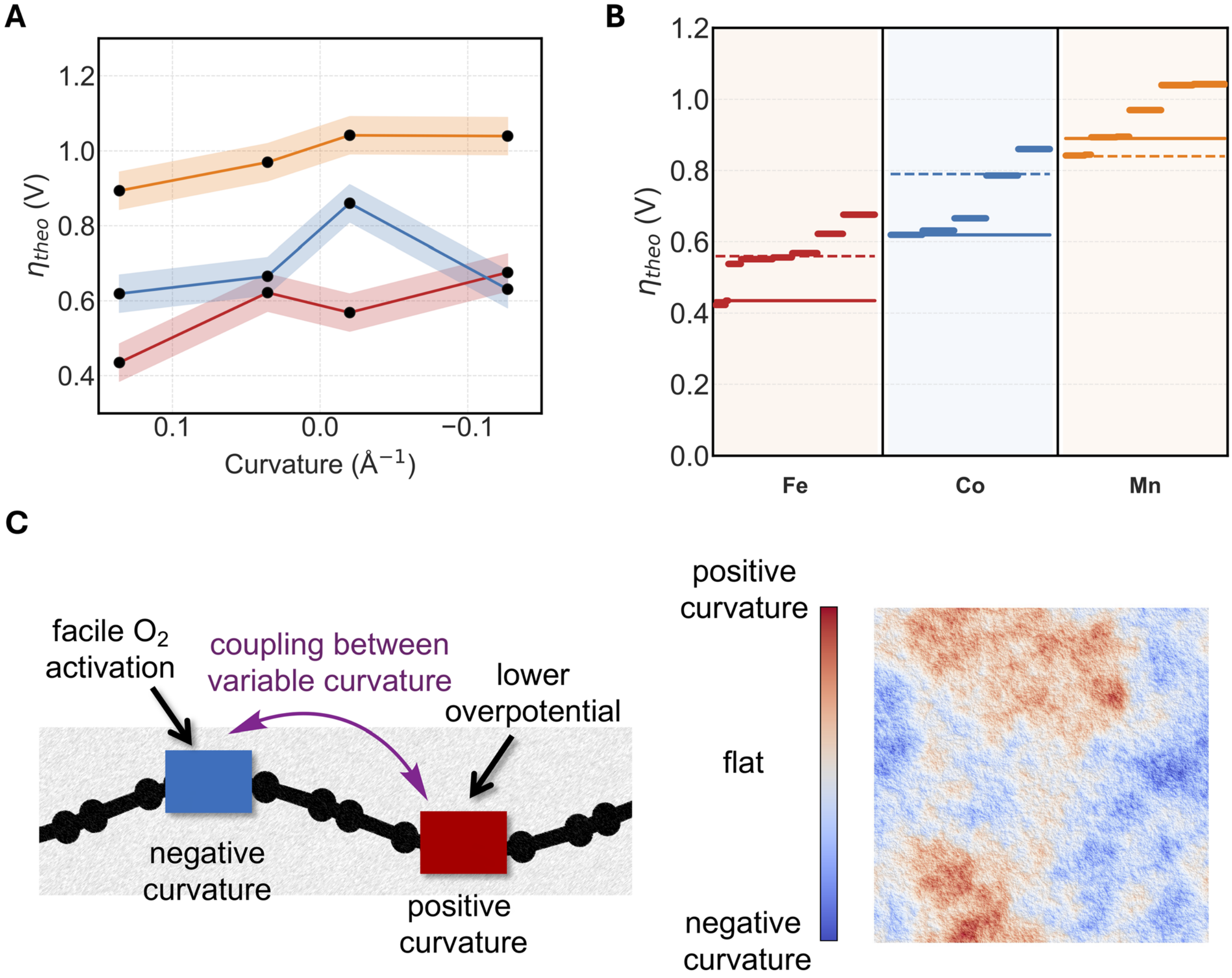

Fig. 6 (A) Variation of the calculated overpotential (η_{theo}) as a function of curvature for Fe, Co, and Mn M–N–C catalysts. For Pt, see SI. (B) Effect of variable curvature on the overpotential. The dashed line denotes the overpotential for the flat-surface MN_4 sites, whereas the solid line represents the lowest overpotential obtained from (A) for each metal. In all cases, deviations from the flat-surface overpotential occur in the presence of surface corrugation. (C) A schematic representation illustrating the coupling between regions of different curvature to model a corrugated surface with variable curvature. This schematic is not based on a specific modeled or experimentally observed surface, but rather serves as a conceptual framework to convey that the presence of corrugation can influence catalytic performance.

Role of variable curvature on the overpotential

We now introduce the concept of variable curvature-driven overpotential tuning, where catalytic sites located at regions of different curvature can interact and exchange intermediates (see page 12–13 in the SI). In this framework, we consider a hypothetical surface composed of a mixture of flat, positively curved, and negatively curved M–N–C sites that together form a multi-curvature reaction network. Within this network, different elementary steps of the ORR are allowed to occur on distinct curvature regions, representing the possible spatial and temporal heterogeneity of real catalytic surfaces under reaction conditions. Specifically, we evaluate the overall limiting potential by sampling combinations of ΔG values for the four ORR steps at five curvature positions—two positive, two negative, and one flat (zero curvature)—for each metal center. It is important to note that this analysis does not capture dynamic ripple formation or explicit diffusion processes; in other words, the actual mode of communication across different curvature sites is not modeled here. Rather, the objective is to demonstrate that dynamic ripples, which are known to exist in these systems, can influence the overpotential. Moreover, experimental measurements typically report ensemble-averaged values that may inherently include contributions from regions of different curvature.

Through this multi-site interaction model, we observe a significant variation in the calculated η_{theo} compared to the static, single-curvature and flat surfaces (Fig. S10). In general, we observe variations relative to flat surfaces, implying the need for an ensemble-averaged framework that accounts for the involvement of sites with variable curvature. In other words, across all metals, mixing of curvature sites produces an appreciable range of η_{theo}, underscoring that catalytic activity on corrugated surfaces cannot be fully represented by a single-site model. Instead, an ensemble average over multiple curvature motifs is necessary. Overall, we predict that on corrugated or dynamically deformed surfaces, cooperative effects between regions of differing curvature can modulate intermediate binding and alter overall reaction energetics.

Conclusions

In summary, we have systematically examined the influence of curvature as a vector descriptor on O_2 activation and the multistep ORR on M–N–C single-atom catalysts. We find that the mechanism of O_2 activation depends on the sign of curvature, enabling selective harnessing of oxygen atoms for orthogonal reactions—such as O-atom transfer *versus* ORR—on chemically identical active sites located at regions of different curvature. The curvature dependence of the ORR overpotential is more pronounced for Mn and Fe than for Co and Pt, where curvature-dependent charge transfer and electrostatic effects can be more effectively exploited. Furthermore, we introduce a variable curvature-interaction model demonstrating that, on corrugated surfaces, the overpotential can be governed by the collective behavior of multiple sites with varying curvature, underscoring the importance of incorporating such structural sampling when predicting experimental observables. Experimental efforts combining *operando* electrochemical measurements with spatially resolved microscopy could provide direct insight into dynamic curvature effects, thereby linking geometric modulation with electronic structure control in catalyst design.

Methods

The adsorption (binding) energies of the ORR intermediates were calculated using the following expressions:

$$\Delta E_{O_2} = E_{O_2^*} - E_{\text{bare}} - E_{O_2}, \tag{1}$$

$$\Delta E_{O} = E_{O^*} - E_{\text{bare}} - E_{O_2} + \frac{1}{2}E_{H_2}, \tag{2}$$

$$\Delta E_{OH} = E_{OH^*} - E_{\text{bare}} - E_{H_2O} + \frac{1}{2}E_{H_2}, \tag{3}$$

$$\Delta E_{OOH} = E_{OOH^*} - E_{\text{bare}} - E_{O_2} - \frac{1}{2}E_{H_2}. \tag{4}$$

Here, E_{bare} denotes the energy of the M–N–C surface, and E_{X^*} represents the energy of the surface with the adsorbed species X (O_2, O, OH, or OOH). E_{O_2} and E_{H_2} correspond to the gas-phase reference energies of O_2 and H_2, respectively. The overall oxygen reduction reaction (ORR) was represented by the following four elementary steps:

$$O_2 + H^+ + e^- + * \rightarrow OOH^*, \tag{5}$$

$$OOH^* + H^+ + e^- \rightarrow O^* + H_2O, \tag{6}$$

$$O^* + H^* + e^- \rightarrow OH^*, \tag{7}$$

$$OH^* + H^* + e^- \rightarrow H_2O + *. \tag{8}$$

The corresponding reaction free energies were determined as:

$$\Delta G_{OOH} = G_{OOH^*} - G_{\text{bare}} - G_{O_2} - \frac{1}{2}G_{H_2}, \tag{9}$$

$$\Delta G_{O} = G_{O^*} - G_{OOH^*} + G_{H_2O} - \frac{1}{2}G_{H_2}, \tag{10}$$

$$\Delta G_{OH} = G_{OH^*} - G_{O^*} + \frac{1}{2}G_{H_2} - G_{H_2O}, \tag{11}$$

$$\Delta G_{H_2O} = G_{H_2O} - G_{OH^*} - \frac{1}{2}G_{H_2}. \tag{12}$$

Here, G_{bare} denotes the Gibbs free energy of the M–N–C surface, and G_{X^*} represents the free energy of the surface with the adsorbed species X. G_{O_2}, G_{H_2}, and G_{H_2O} correspond to the gas-phase reference free energies of O_2, H_2, and H_2O, respectively. All density functional theory (DFT) calculations were performed using the Quantum ESPRESSO software package.[48] The generalized gradient approximation (GGA) with the Perdew–Burke–Ernzerhof (PBE) exchange–correlation functional was employed with ultrasoft GBRV pseudopotentials.[49,50] Dispersion interactions were included *via* the DFT-D3 correction developed by Grimme and co-workers.[51] A (6 × 6) graphene supercell was modeled with a vacuum spacing of approximately 20 Å. One hydrogen atom was placed at the mountain region away from the active sites to maintain consistent rumpling amplitude and sinusoidal curvature across metals and curvature values. More computational details are provided in the SI.

Conflicts of interest

The author declares no competing financial interest.

Data availability

All calculation details required to evaluate the conclusions of this study are available in the supporting information (SI). Structural coordinates used in the calculations can be found in the Banerjee Group GitHub repository (https://github.com/banerjee-group-utk/RSC-Mechanochemistry-2026-d5mr00147a). Supplementary information: additional density functional theory (DFT) calculation details and electronic structure analyses. See DOI: https://doi.org/10.1039/d5mr00147a.

Acknowledgements

This work was supported by startup funds from the University of Tennessee, Knoxville. This research used resources of the National Energy Research Scientific Computing Center, a DOE Office of Science User Facility supported by the Office of Science of the U.S. Department of Energy under Contract No. DE-AC02-05CH11231 using NERSC award NERSC DDR-ERCAP0035235.

References

1 F. L. Thiemann, C. Scalliet, E. A. Müller and A. Michaelides, Defects induce phase transition from dynamic to static rippling in graphene, *Proc. Natl. Acad. Sci. U. S. A.*, 2025, **122**(9), e2416932122.

2 T. P. Darlington, *et al.*, Imaging strain-localized excitons in nanoscale bubbles of monolayer WSe_2 at room temperature, *Nat. Nanotechnol.*, 2020, **15**, 854–860.

3 D. Lloyd, X. Liu, J. W. Christopher, L. Cantley, A. Wadehra, B. L. Kim, B. B. Goldberg, A. K. Swan and J. S. Bunch, Band Gap Engineering with Ultralarge Biaxial Strains in Suspended Monolayer MoS_2, *Nano Lett.*, 2016, **16**, 5836–5841.

4 Y. Gao, F. Deng, R. He and Z. Zhong, Spontaneous curvature in two-dimensional van der Waals heterostructures, *Nat. Commun.*, 2025, **16**, 717.

5 A. Edström, D. Amoroso, S. Picozzi, P. Barone and M. Stengel, Curved Magnetism in CrI_3, *Phys. Rev. Lett.*, 2022, **128**, 177202.

6 D. W. Boukhvalov and M. I. Katsnelson, Enhancement of Chemical Activity in Corrugated Graphene, *J. Phys. Chem. C*, 2009, **113**, 14176–14178.

7 M. A. Bissett, S. Konabe, S. Okada, M. Tsuji and H. Ago, Enhanced Chemical Reactivity of Graphene Induced by Mechanical Strain, *ACS Nano*, 2013, **7**, 10335–10343.

8 Y. Shen, E. Dai, X. Liu, W. Pan, H. Yang, B. Xiong and D. Zerulla, Curvature analysis of single layer graphene on the basis of extreme low-frequency Raman spectroscopy, *Appl. Phys. Lett.*, 2019, **114**(16), 161907.

9 S. Deng, D. Rhee, W.-K. Lee, S. Che, B. Keisham, V. Berry and T. W. Odom, Graphene Wrinkles Enable Spatially Defined Chemistry, *Nano Lett.*, 2019, **19**, 5640–5646.

10 D. Perco, M. Pozzo, M. Bianchi, P. Lacovig, F. Sammartino, P. Hofmann, S. Lizzit, D. Alfè and A. Baraldi, Anisotropy-driven double corrugation: Coexistence of one- and two-dimensional wave patterns in epitaxial graphene on iridium, *Carbon*, 2026, **246**, 120934.

11 S. Stavrić, V. Chesnyak, S. del Puppo, M. Panighel, G. Comelli, C. Africh, Ž. Šljivančanin and M. Peressi, 1D selective confinement and diffusion of metal atoms on graphene, *Carbon*, 2023, **215**, 118486.

12 N. Hawthorne, E. J. Broker, Y. Bao, S. Banerjee, Q. Moore, C. Cardinal, J. Ha, U. D. Braga, A. M. Rappe and J. D. Batteas, Studies of the mechanically induced reactivity of graphene with water using a 2D-materials strain reactor, *Mater. Horiz.*, 2025, **12**, 1179–1188.

13 M. Ackerman, P. Kumar, M. Neek-Amal, P. Thibado, F. Peeters and S. Singh, Anomalous Dynamical Behavior of Freestanding Graphene Membranes, *Phys. Rev. Lett.*, 2016, **117**, 126801.

14 J. K. Schoelz, P. Xu, V. Meunier, P. Kumar, M. Neek-Amal, P. M. Thibado and F. M. Peeters, Graphene ripples as a realization of a two-dimensional Ising model: A scanning tunneling microscope study, *Phys. Rev. B:Condens. Matter Mater. Phys.*, 2015, **91**(4), 045413.

15 M. Neek-Amal, P. Xu, J. Schoelz, M. Ackerman, S. Barber, P. Thibado, A. Sadeghi and F. Peeters, Thermal mirror buckling in freestanding graphene locally controlled by scanning tunnelling microscopy, *Nat. Commun.*, 2014, **5**, 4962.

16 Y. Zhang, T. Gao, Y. Gao, S. Xie, Q. Ji, K. Yan, H. Peng and Z. Liu, Defect-like Structures of Graphene on Copper Foils for Strain Relief Investigated by High-Resolution Scanning Tunneling Microscopy, *ACS Nano*, 2011, **5**, 4014–4022.

17 M. Van Winkle, K. Zhang and D. K. Bediako, Nanoscale Structure and Interfacial Electrochemical Reactivity of Moiré-Engineered Atomic Layers, *Acc. Chem. Res.*, 2025, **58**, 415–427.

18 P. Li, W. Y. Wang, X. Sui, X. Fan and J. Li, Effects of moiré lattice distortion and bond on the superlubricity of twist MoS_2/graphene and MoS_2/BN heterointerfaces, *J. Mater. Sci. Technol.*, 2024, **196**, 125–136.

19 L. Liu and A. Corma, Metal Catalysts for Heterogeneous Catalysis: From Single Atoms to Nanoclusters and Nanoparticles, *Chem. Rev.*, 2018, **118**, 4981–5079.

20 H.-Y. Zhuo, X. Zhang, J.-X. Liang, Q. Yu, H. Xiao and J. Li, Theoretical Understandings of Graphene-based Metal Single-Atom Catalysts: Stability and Catalytic Performance, *Chem. Rev.*, 2020, **120**, 12315–12341.

21 J. K. Nørskov, F. Studt, F. Abild-Pedersen and T. Bligaard, *Fundamental Concepts in Heterogeneous Catalysis*, Wiley, 2014.

22 J. K. Nørskov, J. Rossmeisl, A. Logadottir, L. Lindqvist, J. R. Kitchin, T. Bligaard and H. Jónsson, Origin of the Overpotential for Oxygen Reduction at a Fuel-Cell Cathode, *J. Phys. Chem. B*, 2004, **108**, 17886–17892.

23 A. Cao, V. J. Bukas, V. Shadravan, Z. Wang, H. Li, J. Kibsgaard, I. Chorkendorff and J. K. Nørskov, A spin promotion effect in catalytic ammonia synthesis, *Nat. Commun.*, 2022, **13**, 2382.

24 A. Kakekhani, S. Ismail-Beigi and E. I. Altman, Ferroelectrics: A pathway to switchable surface chemistry and catalysis, *Surf. Sci.*, 2016, **650**, 302–316.

25 M. A. Ardagh, O. A. Abdelrahman and P. J. Dauenhauer, Principles of Dynamic Heterogeneous Catalysis: Surface Resonance and Turnover Frequency Response, *ACS Catal.*, 2019, **9**, 6929–6937.

26 T. V. Cleve, S. Moniri, G. Belok, K. L. More and S. Linic, Nanoscale Engineering of Efficient Oxygen Reduction Electrocatalysts by Tailoring the Local Chemical Environment of Pt Surface Sites, *ACS Catal.*, 2016, **7**, 17–24.

27 A. Holewinski, J.-C. Idrobo and S. Linic, High-performance Ag–Co alloy catalysts for electrochemical oxygen reduction, *Nat. Chem.*, 2014, **6**, 828–834.

28 R. B. Wexler, J. M. P. Martirez and A. M. Rappe, Chemical Pressure-Driven Enhancement of the Hydrogen Evolving Activity of Ni_2P from Nonmetal Surface Doping Interpreted *via* Machine Learning, *J. Am. Chem. Soc.*, 2018, **140**, 4678–4683.

29 J. Su, *et al.*, Strain enhances the activity of molecular electrocatalysts *via* carbon nanotube supports, *Nat. Catal.*, 2023, **6**, 818–828.

30 Y. Wang, Z. Bao, M. Shi, Z. Liang, R. Cao and H. Zheng, The Role of Surface Curvature in Electrocatalysts, *Chem. - Eur. J.*, 2022, **28**, e202102915.

31 C. Liu, Q. Chen, Z. Chen, J. Wang, H. Wang, L. Luo, X. Li, Q. Jiang, T. Zheng and C. Xia, Substrate Curvature Enhances Molecular Electrocatalysts for the Efficient Production of Hydrogen Peroxide, *Nano Lett.*, 2025, **25**(44), 16013–16019.

32 M. Weh, A. A. Kroeger, O. Anhalt, A. Karton and F. Würthner, Mutual induced fit transition structure stabilization of corannulene's bowl-to-bowl inversion in a perylene bisimide cyclophane, *Chem. Sci.*, 2024, **15**, 609–617.

33 R. Cepitis, N. Kongi, J. Rossmeisl and V. Ivaništšev, Surface Curvature Effect on Dual-Atom Site Oxygen Electrocatalysis, *ACS Energy Lett.*, 2023, **8**, 1330–1335.

34 A. Kulkarni, S. Siahrostami, A. Patel and J. K. Nørskov, Understanding Catalytic Activity Trends in the Oxygen Reduction Reaction, *Chem. Rev.*, 2018, **118**, 2302–2312.

35 H. T. Chung, D. A. Cullen, D. Higgins, B. T. Sneed, E. F. Holby, K. L. More and P. Zelenay, Direct atomic-level insight into the active sites of a high-performance PGM-free ORR catalyst, *Science*, 2017, **357**, 479–484.

36 G. Wu, K. L. More, C. M. Johnston and P. Zelenay, High-Performance Electrocatalysts for Oxygen Reduction Derived from Polyaniline, Iron, and Cobalt, *Science*, 2011, **332**, 443–447.

37 S. Yu, Z. Levell, Z. Jiang, X. Zhao and Y. Liu, What Is the Rate-Limiting Step of Oxygen Reduction Reaction on Fe–N–C Catalysts?, *J. Am. Chem. Soc.*, 2023, **145**, 25352–25356.

38 Y. He, S. Liu, C. Priest, Q. Shi and G. Wu, Atomically dispersed metal–nitrogen–carbon catalysts for fuel cells: advances in catalyst design, electrode performance, and durability improvement, *Chem. Soc. Rev.*, 2020, **49**, 3484–3524.

39 R. Jasinski, A New Fuel Cell Cathode Catalyst, *Nature*, 1964, **201**, 1212–1213.

40 K. Kim, G. Kim, T. Jeong, W. Lee, Y. Yang, B.-H. Kim, B. Kim, B. Lee, J. Kang and M. Kim, Activating the Mn Single Atomic Center for an Efficient Actual Active Site of the Oxygen Reduction Reaction by Spin-State Regulation, *J. Am. Chem. Soc.*, 2024, **146**, 34033–34042.

41 H. Fei, *et al.*, General synthesis and definitive structural identification of MN_4C_4 single-atom catalysts with tunable electrocatalytic activities, *Nat. Catal.*, 2018, **1**, 63–72.

42 Kment, A. Bakandritsos, I. Tantis, H. Kmentová, Y. Zuo, O. Henrotte, A. Naldoni, M. Otyepka, R. S. Varma and R. Zbořil, Single Atom Catalysts Based on Earth-Abundant Metals for Energy-Related Applications, *Chem. Rev.*, 2024, **124**, 11767–11847.

43 S. Hong, K. D. Sutherlin, J. Park, E. Kwon, M. A. Siegler, E. I. Solomon and W. Nam, Crystallographic and spectroscopic characterization and reactivities of a mononuclear non-haem iron(III)-superoxo complex, *Nat. Commun.*, 2014, **5**, 5440.

44 A. Karlsson, J. V. Parales, R. E. Parales, D. T. Gibson, H. Eklund and S. Ramaswamy, Crystal Structure of Naphthalene Dioxygenase: Side-on Binding of Dioxygen to Iron, *Science*, 2003, **299**, 1039–1042.

45 F. Calle-Vallejo, J. I. Martínez, J. M. García-Lastra, J. Rossmeisl and M. T. M. Koper, Physical and Chemical Nature of the Scaling Relations between Adsorption Energies of Atoms on Metal Surfaces, *Phys. Rev. Lett.*, 2012, **108**(11), 116103.

46 F. Calle-Vallejo, A. Krabbe and J. M. García-Lastra, How covalence breaks adsorption-energy scaling relations and solvation restores them, *Chem. Sci.*, 2017, **8**, 124–130.

47 F. Abild-Pedersen, J. Greeley, F. Studt, J. Rossmeisl, T. R. Munter, P. G. Moses, E. Skúlason, T. Bligaard and J. K. Nørskov, Scaling Properties of Adsorption Energies for Hydrogen-Containing Molecules on Transition-Metal Surfaces, *Phys. Rev. Lett.*, 2007, **99**(1), 016105.

48 P. Giannozzi, *et al.*, Quantum ESPRESSO: a modular and open-source software project for quantum simulations of materials, *J. Phys.: Condens. Matter*, 2009, **21**, 395502.

49 J. P. Perdew, K. Burke and M. Ernzerhof, Generalized Gradient Approximation Made Simple, *Phys. Rev. Lett.*, 1996, **77**, 3865–3868.

50 K. F. Garrity, J. W. Bennett, K. M. Rabe and D. Vanderbilt, Pseudopotentials for high-throughput DFT calculations, *Comput. Mater. Sci.*, 2014, **81**, 446–452.

51 S. Grimme, J. Antony, S. Ehrlich and H. Krieg, A consistent and accurate *ab initio* parametrization of density functional dispersion correction (DFT-D) for the 94 elements H-Pu, *J. Chem. Phys.*, 2010, **132**(15), 154104.